Shear banding mechanism in compressed nanocrystalline ceramic nanopillars

Haw-Wen Hsiao,[1] Shu Li,[2] Karin A. Dahmen,[2] and Jian-Min Zuo [1,*]

[1]*Department of Materials Science and Engineering, University of Illinois at Urbana-Champaign, Urbana, Illinois 61801, USA*
[2]*Department of Physics, University of Illinois at Urbana-Champaign, Urbana, Illinois 61801, USA*

Localization of deformation in shear bands is widely observed preceding intense damage and fracture in ductile or granular materials. However, mechanisms about how shear bands form are generally not known. Here, we show that nanocrystalline ceramic (NCC) nanopillars of ZrN fracture by shear banding under compression. The microstructure evolution of entire shear banding process was *in situ* monitored by electron imaging and diffraction. Results show that the nanopillars deform through a series of granular activities due to intermittent nucleation and propagation of dislocations. The stress drops associated with the dislocation activities are relatively small since dislocation avalanches are restricted in NCCs because of the effect of nanograin size. Localized and cooperative granular activities, as well as nanocracks, are discovered in the regions where shear bands form. A model about shear band and nanocrack formation is proposed. These findings thus demonstrate for the first time of spatial and temporal nature of intermittent granular activities, leading to shear band formation in NCCs.

I. INTRODUCTION

Shear banding causes deformation to be heavily restricted in small volumes of a material, which are broadly referred to as shear bands. Such restrictions are observed in rolled metals [1], metallic glasses [2,3], granular materials [4,5], and nanocrystalline metals (NCMs) [6–9]. The bifurcation from uniform deformation to localized deformation significantly alters the material's mechanical response. The onset of shear bands represents initial plastic yielding and induces a highly localized plastic flow that limits ductility. For this reason, shear bands have attracted tremendous interest in the study of metallic glasses [2,3] and NCMs [10].

Shear bands in general are not observed in brittle ceramic materials. Plasticity including superplasticity is variously observed in nanocrystalline ceramics (NCCs) [11] and even at low temperatures [12,13], and shear banding has been reported in NCC thin films of different compositions and microstructures [14–16].

NCC materials are strengthened by the smaller grain sizes that follow the Hall-Petch relationship, where the yielding strength of a material is inversely proportional to the square root of its grain size. As the grain sizes further reduce, grain boundaries (GBs) provide another path to accommodate the applied stress leading to softening below a critical grain size [9,17–20], which is known as the inverse Hall-Petch relation [10]. The breakdown of Hall-Petch relation in NCCs was recently demonstrated to be strongly correlated with the grain boundary volume fraction in nanocrystalline magnesium aluminate ($MgAl_2O_4$) spinel [20]. Earlier study by Szlufaraka *et al.* [21] discovered the crossover of deformation mechanisms at the onset of grain boundary yielding. Both studies suggested the prominent effect of grain boundaries on the deformation behavior of NCCs. There are several GB-mediated deformation mechanisms, including GB migration [22], GB sliding [7], grain rotation [23], and twinning [24]. These mechanisms provide additional plasticity essential to engineering applications. However, how these mechanisms operate and how they contribute to shear banding in NCCs are unanswered questions.

In situ observation is critical to elucidate the underlying deformation mechanisms. Such study is very limited so far. Recently, Pagan *et al.* reported on a study of shear band formation in single-crystal copper using high-resolution x-ray diffraction [25]. Single-crystal orientation pole figures were generated from the diffraction data, which are used to track the distribution of lattice orientations and its development during the process of slip localization. The diffraction method employed is very sensitive to the changes in microstructure, and the interpretation of the diffraction data was helped by the measurement of the strain fields on the sample surface simultaneously using digital image correlation (DIC) [25].

Here, we show that the NCC nanopillars of zirconium nitride (ZrN) deform under compression by shear banding. Using *in situ* transmission electron microscopy (TEM) observations, we followed the shear banding process using electron imaging or diffraction. By monitoring microstructural response *in situ*, we are able to observe the embryonic state of shear bands and associated granular activities at high spatial resolution for insights into the formation of shear bands.

II. EXPERIMENTAL METHODS

The material used in this investigation is the nanocrystalline thin film of zirconium nitride (ZrN). To observe granular activities, we performed nanopillar compression test inside a JEOL 2010 LaB_6 TEM (JEOL USA, Peabody, MA) using

---

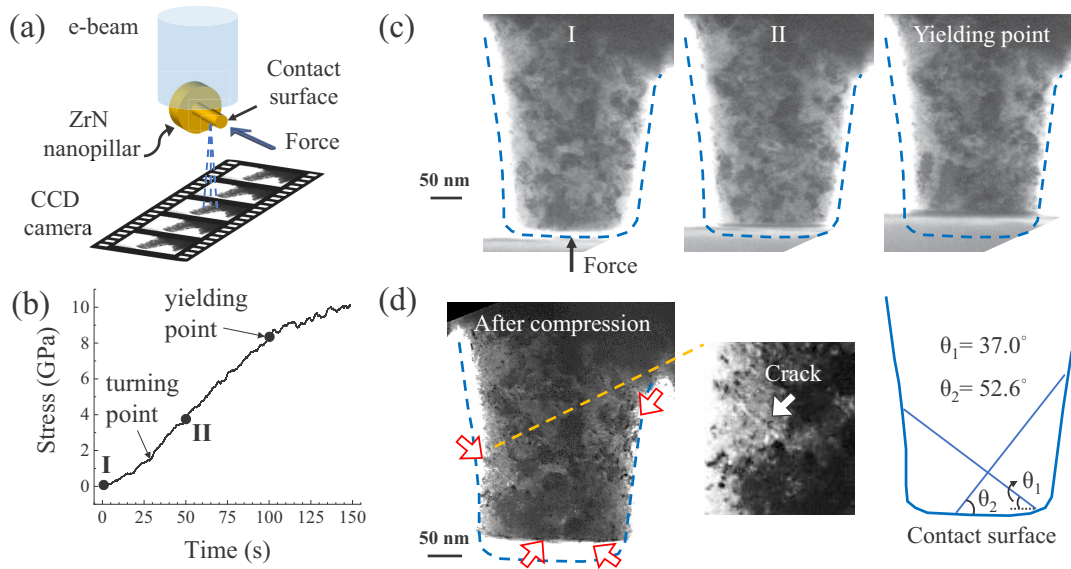*Corresponding author: jianzuo@illinois.edu

FIG. 1. *In situ* nanopillar compression test using bright-field TEM imaging. (a) A schematic diagram of the nanopillar compression test performed inside a TEM. (b) The measured stress-time curve for nanopillar A. Two slope changes in the stress-time curve are marked, as well as the selected points I and II. (c) The image frames recorded at the points I and II and the yielding point in (b). (d) A TEM image of nanopillar A taken after the compression. The arrows mark two observed shear bands and nanocrack. The schematic diagram indicates the location and orientation of the observed slip bands as well as the contact surface with the indenter probe.

the setup illustrated in Fig. 1(a). The ZrN thin film (average grain size of 18 nm) was deposited on a single-crystal silicon substrate by the unbalanced magnetron sputtering method [26]. Nanopillars were fabricated in the plane-view direction of the thin film by the focused ion beam (FIB) method, and mounted onto a molybdenum TEM grid. The acceleration voltage of the Ga ion gun was kept at 30 kV during the entire FIB process, while the final milling was performed at the low current of 7.7 pA to reduce the milling damage. The nanopillars described here are named as nanopillar A, B, and C, of diameters of 240, 120, and 150 nm, respectively.

The compression test was carried out using a Hysitron PI95 picoindenter holder (Hysitron, Eden Prairie, MN) at the data acquisition rate of 400 Hz. A feedback loop between the transducer controller and transducer was utilized to set the desired displacement rate, in the so-called "displacement control" mode, where the transducer controller adjusts the applied force to keep the displacement rate close to its targeted setting. The targeted strain rate of the nanopillar was at 10^{-3} s^{-1}, and the indenter mechanical response was monitored by the stress-time and strain-time curves. An example of the stress-time curve is shown in Fig. 1(b) for nanopillar A.

In addition to monitoring the mechanical response, electron bright-field images or diffraction patterns were simultaneously captured in a video at the frame rate of 10 frames/s during deformation, using a charge-coupled-device camera (Model Orius, Gatan, CA). Figure 1(c) shows several examples of the captured frames (the video is provided in Ref. [27]).

Time resolved diffraction patterns were recorded using a parallel electron beam of 200 nm in diameter. The individual diffraction spots were identified and traced to specific nanograins using the identification method described

in Ref. [27], with the help of scanning electron nanodiffraction (SEND) [28].

The granular activity was followed using following methods.

(1) *The difference image method.* The method detects the change in the recorded image. Since the image contrast is sensitive to diffraction condition, the change indicates the location and as well as the extent of granular activity. The difference image is calculated by first selecting two image frames, $f1$ and $f2$, at a time of τ apart ($\tau = 1.0$ s here). Each selected image is then averaged with its neighboring two frames (± 0.1 s) to obtain $\overline{f1}$ and $\overline{f2}$ to reduce the image noise. The difference image is then obtained by calculating the absolute difference of $|\overline{f1} - \overline{f2}|$. The brighter contrast regions in the difference image indicate granular activities.

(2) *The integrated intensity method.* In the integrated intensity method, the background noise in a difference image is filtered out using a custom MATLAB script by following the method described in Ref. [27], and only the strong signals in the filtered image are kept. The integrated intensity $|\Delta I|$ is then obtained by summing the pixel intensity of the filtered difference image.

(3) *The cumulative difference (CD) image.* The CD image is obtained by averaging all of the difference image frames in a specified time period, for example, from the beginning (0 s) to time t. The frames are filtered using the same method for integrated intensity method to reduce the background noise.

(4) *Diffraction spot motion.* The diffraction spot moves and changes intensity as the grain rotates or deforms, where circular movement is responsible for the in-plane grain rotation; distance variation between the diffraction spot and the transmitted beam reflects lattice strain within a grain. Activities of a grain can also be qualitatively monitored from

the corresponding diffraction spot intensity since the intensity is determined by the diffraction condition which changes as the grain tilts or deforms.

(5) *The diffraction pattern correlation method.* The diffraction pattern as whole also carries the information about microstructure inside the nanopillar. The difference between two diffraction patterns thus can be used to monitor the change in the microstructure during deformation. The change in diffraction patterns can be quantified using the correlation coefficient between two patterns. The contributions from the transmitted beam and background noises were removed in the calculation following the method described in Ref. [27]. The correlation coefficient r is computed by the following equation:

$$r = \frac{\sum_m \sum_n (A_{mn} - \bar{A})(B_{mn} - \bar{B})}{\sqrt{\left(\sum_m \sum_n (A_{mn} - \bar{A})^2\right)\left(\sum_m \sum_n (B_{mn} - \bar{B})^2\right)}},$$

where r is the correlation coefficient, whose value ranges from 1 to -1, with 1 for two identical patterns and -1 for two patterns opposite in contrast; m and n are the row/column coordinate of a pixel in a pattern; A and B are the pixel intensities at (m, n) in the two patterns; $\bar{A}$ and $\bar{B}$ are the mean intensities of two patterns. Application examples of the above methods will be illustrated in the next section.

III. RESULTS

A. Nanopillar deformation under compressive stress

A representative example of the measured stress during nanopillar deformation is shown in Fig. 1(b) for nanopillar A. The stress-time curve is relatively smooth without large stress drops that are often associated with dislocation avalanches [29]. The turning point and the yielding point in Fig. 1(b) mark where a significant change in the slope is seen. Figure 1(c) shows the captured images at points I and II that are marked on the stress-time curve, and at the yielding point. These images together with the captured video (video 1 in Ref. [27]) show that the nanopillar deforms continuously without brittle fracture. An inspection of the video also indicates that the image contrast inside the nanopillar frequently changes during the deformation, and the nanopillar finally fails via shear banding along the slip bands marked in Fig. 1(d). The bright-field image in Fig. 1(d) was taken after the compression, where the slip bands are marked by arrows, and the nanocrack associated with the slip band is highlighted. The slip bands are at 37.0° and 52.6° to the pillar contact surface, respectively.

The nanopillar A was compressed twice, the maximum strain reached during the first compression was 16%. The second compression on nanopillar A was recorded as video 2 [27], showing that the crystalline nanograins initially remained static without significant image contrast change inside the nanopillar. As the applied stress approached the yielding point, nanopillar began to slip with frequent contrast change along the observed shear bands. The yielding stresses are approximately same in both compressions.
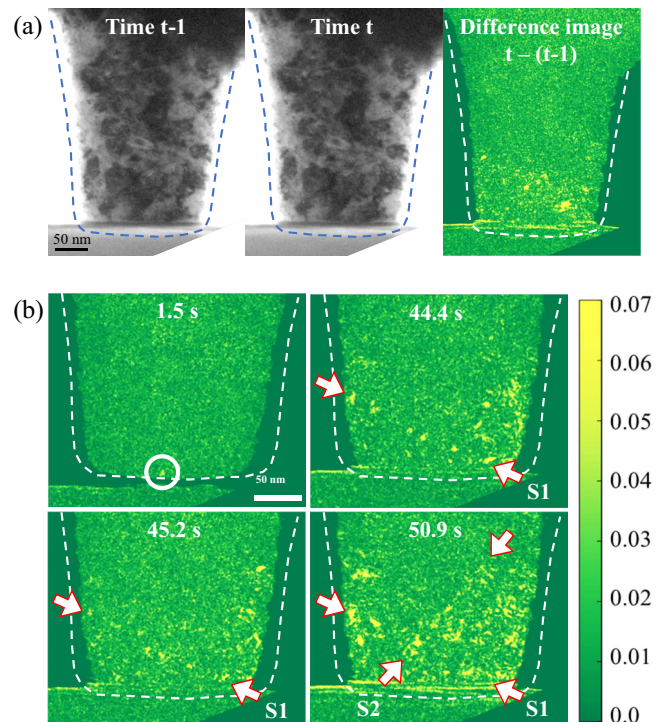

FIG. 2. Observation of granular activities using the difference image method. (a) An example of two bright-field images recorded at 1.0 s time interval apart, and their difference image. (b) The selected difference images obtained during the deformation of nanopillar A. The arrows indicate where the connected granular activities and along the shear bands (S1 and S2) are observed. The time marked on the image is the starting time of the difference image.

B. Granular activities observed by the difference image method and the onset of shear band formation

We used the difference image method described in the method section to monitor granular activities. An example of the difference image is shown in Fig. 2(a), where two as-recorded images at 1.0 s apart and their difference image are shown. Figure 2(b) highlights the granular activities as observed by this method during the compression of nanopillar A. The granular activity was first detected after 1.5 s near the contact between the nanopillar and the indenter as marked by the circle in Fig. 2(b), demonstrating that granular activities take place at a relatively low applied stress. Connected granular activities were detected at 44.4 s (indicated by arrows and labelled as S1). This was followed by additional activities along S1, as demonstrated by the difference image at 45.2 s. At 50.9 s, new connected granular activities were detected along the line marked as S2. The two marked lines of S1 and S2 are positioned close to the two slip bands of Fig. 1(d) (also see Fig. S3 in Ref. [27]), suggesting that the connected granular activities are associated with the formation of the embryos of the shear bands, and $t_1 = 44.4$ s and $t_2 = 50.9$ s mark the onset of the shear band formation in nanopillar A.

C. Intermittent granular activities during deformation

The integrated intensity method described in the method section was used to monitor the intermittency of
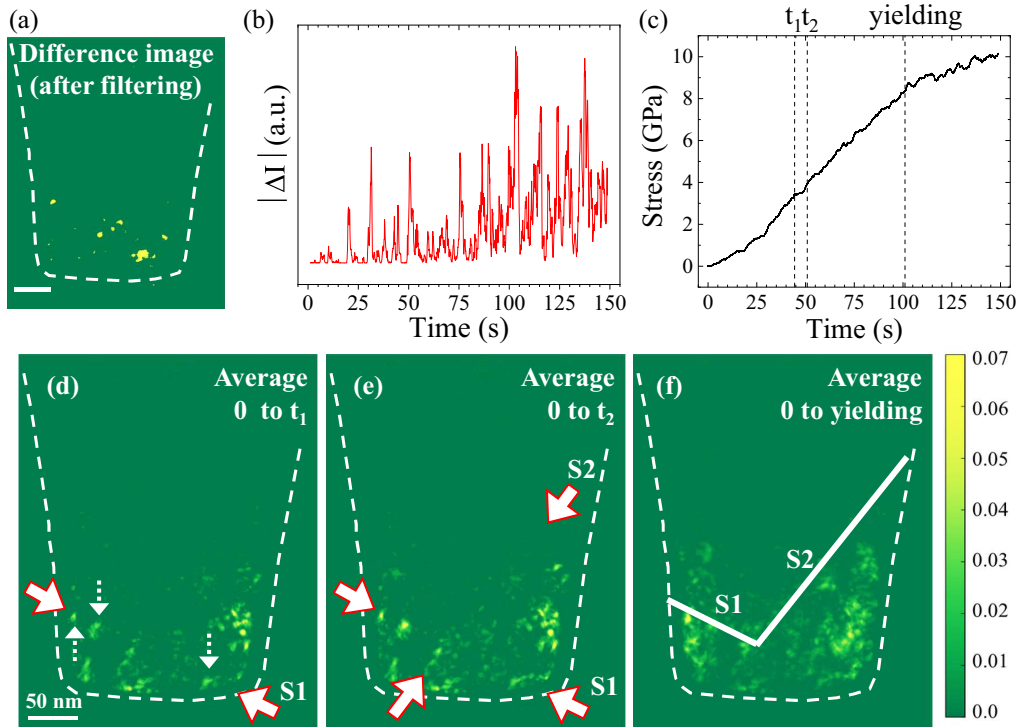
FIG. 3. Intermittent granular activities detected by the integrated intensity method. (a) Example difference image from Fig. 2(a) after background noise filtering. Scale bar: 50 nm. (b) Integrated intensity of the filtered difference images as function of time for nanopillar A. (c) A plot of the stress-time curve for the same time period as in (b). Here, t_1, t_2, and the yielding point are defined in Figs. 1(b) and 2(b). [(d), (e), and (f)] The integrated images from 0 s to t_1, t_2, and yielding point, respectively, showing the cumulative granular activities during the different periods of time. The solid arrows and solid lines mark the locations of S1 and S2.

granular activities. Figure 3(a) show a difference image after noise filtering. The sum of the difference image intensity was then plotted as function of time in Fig. 3(b). The result demonstrates intermittent granular activities taking place throughout the deformation. By comparing with the stress-time curve [Fig. 3(c)], the intensity of granular activities is seen to become stronger after the yielding point, indicating that the amount of granular activities was enhanced as the nanopillar started yielding. However, interestingly, significant granular activities also occurred before yielding.

An examination of the location as well as the intensity of granular activities is provided by the CD image method. Three CD images are displayed in Figs. 3(d)–3(f), showing cumulative granular activities in the three different periods of time. Figure 3(d), for instance, is from 0 s to t_1 as marked in Fig. 3(c). Solid arrows indicate the locations of S1 and S2. The brighter areas are where the granular activities have taken place more often. The granular activities are mostly concentrated in few regions. Along S1, some grains have more activities (indicated by dash arrows) than others, implying that these grains operated multiple times prior to the onset of shear band formation. A similar situation is also observed for S2 [Fig. 3(e)]. From the beginning to the yielding point, most of the granular activities are distributed between S1, S2, and the contact (C) between the indenter and the nanopillar [Fig. 3(f)]. Only few granular activities are observed beyond S1 and S2.

D. Dislocation activities during nanopillar compression

To better understand how the nanopillar responds to compressive stresses, a small diameter ($\sim$120 nm) nanopillar sample (nanopillar B) was prepared and tested. The smaller sample provided clear image contrast inside the nanopillar, which is shown in Fig. 4. The entire deformation process was captured as video 3 in Ref. [27]. Several video frames are selected and shown in Fig. 4 to demonstrate the dislocation activities during compression. The video shows that dislocations were activated at 9.7 s near the contact between the nanopillar and the indenter probe, where the stress is greatest because of the geometrical confinement of stress and stress gradient according to the finite element simulations [29]. The dislocations then propagated and interacted with each other from 9.7 to 24.8 s and finally form a dislocation network as the stress flows away from the contact surface.

In the bottom panel of Fig. 4, the darkening contrast of dislocations was seen at 29.0 s. The darkening can be attributed to the formation of a dense dislocation network, and because of the increased dislocation density, resolving individual dislocations was no longer possible. The dislocation network then propagated upward and temporarily stopped at 38.0 s. Afterward, the dislocation network moved little, and the contrast changed frequently suggesting dislocation activities associated with plastic deformation. The shear band was clearly observed in nanopillar B at 66.2 s.
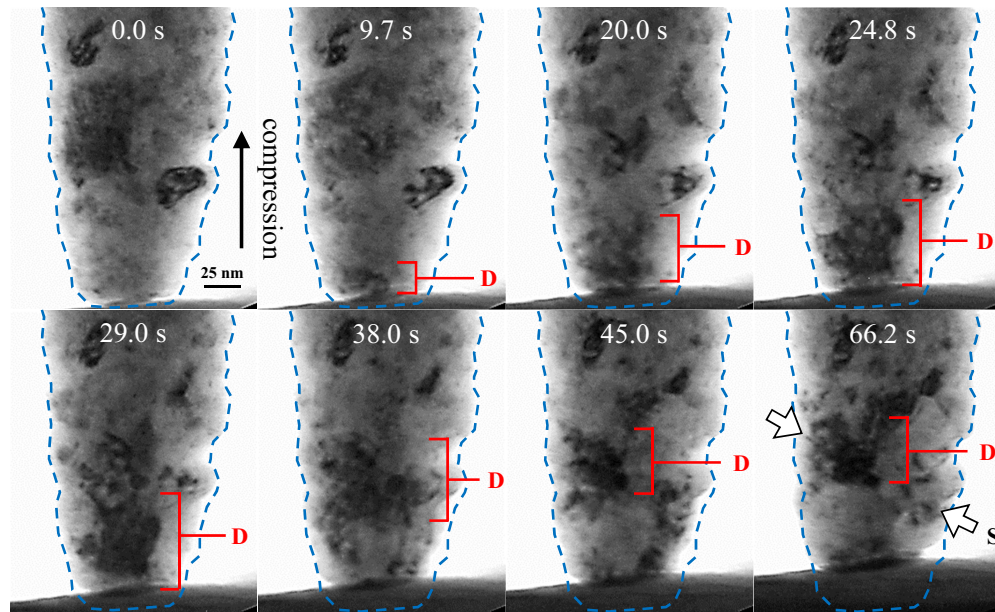
FIG. 4. Snapshots of *in situ* video recorded from for nanopillar B during compressive deformation. Symbol D indicates the dislocation propagation and the development of dislocation activities.

E. Grain deformation and rotations

To provide quantitative information on granular activities, we performed an *in situ* compression test in diffraction mode. By tracking and measuring individual diffraction spot position, we can monitor the strain as well as in-plane grain rotation. Three nanograins marked as G1, G2, and G3 were monitored inside a nanopillar of 150 nm in diameter (nanopillar C). All three nanograins are near the shear band that was later observed in the nanopillar. The locations and the shapes of three nanograins were determined by SEND and marked on the bright-field image of as-fabricated sample (as shown in Fig. S4 [27]). The details of grain identification are described in Ref. [27]. Figure 5(a) displays the stress-time curve of nanopillar C, whose yielding point is marked by the arrow. As shown in Fig. 5(b), G1 and G2 began to rotate at the yielding point, while the rotation of G3 slowly increased soon after the deformation. The stepped curve indicates that the process is intermittent. The significant increase in grain rotation after yielding suggests that the enhancement was induced by shear banding.

The lattice strain was measured together with the in-plane rotation angle from the position of the selected diffraction spot, following the method described in Ref. [27]. The direction of the measured strain is indicated by the arrows in Fig. S4. The lattice strain variations inside the nanograins with time are shown in Fig. 5(c). The noise indicates the measurement error, which is largely due to the inhomogeneous intensity inside the diffraction spot during deformation. The lattice strains start to develop after 40 s. Among the three observed grains, G1 developed a compressive strain, the strain in G2 was tensile, indicating bending or buckling, and the strain in G3 started to develop at 90 s.

Figure 5(d) plots the diffraction spot intensity of G1, G2, and G3 nanograins during deformation. Since the diffraction spot intensity is determined by the volume of the grain, its

diffraction condition and strain, we expect a change to occur once the diffraction condition and strain are modified by granular activities. In Fig. 5(d), the diffraction spot intensity of G1 increased first and started to decrease at 40 s, while the change in the diffraction spot intensity of G2 and G3 is smaller. By contrast, the rotation angle measurement showed very little in-plane rotation for G1 and G2 up to the yielding point. This result shows that the diffraction spot intensity is more sensitive to granular activities than the direct in-plane rotation measurement. The continuous change in intensity observed in all three grains indicates that granular activities constantly occurred during deformation, which modified the diffraction condition. Since the amount of strain and rotation are both small prior to the yielding point, the modification of diffraction condition can be attributed to small out-of-plane tilt.

F. Monitoring overall microstructure evolution using diffraction

Figure 6 shows the correlation map of the diffraction patterns recorded as nanopillar C was compressed, calculated using the diffraction pattern correlation method described in the methods section. Both the horizontal and vertical axes of the 2D map represent the time. The value at the coordinate (t_a, t_b) represents the correlation coefficient between two patterns recorded at times t_a and t_b. The change in microstructure increases with the increasing time difference, such that the correlation coefficient is highest ($t_a = t_b$, $r = 1$) along the 45° direction and decays as we move away from the 45° axis. The high r values are presented in dark red color in Fig. 6. The width of the red band in the correlation map represents the speed of microstructure modification during deformation. Two major band width reductions (dark and bright red) are found in Fig. 6, and they are marked as R1 and R2. Both imply that microstructure modification was accelerated. R1 and R2 are attributed to the onset of shear band formation and shear
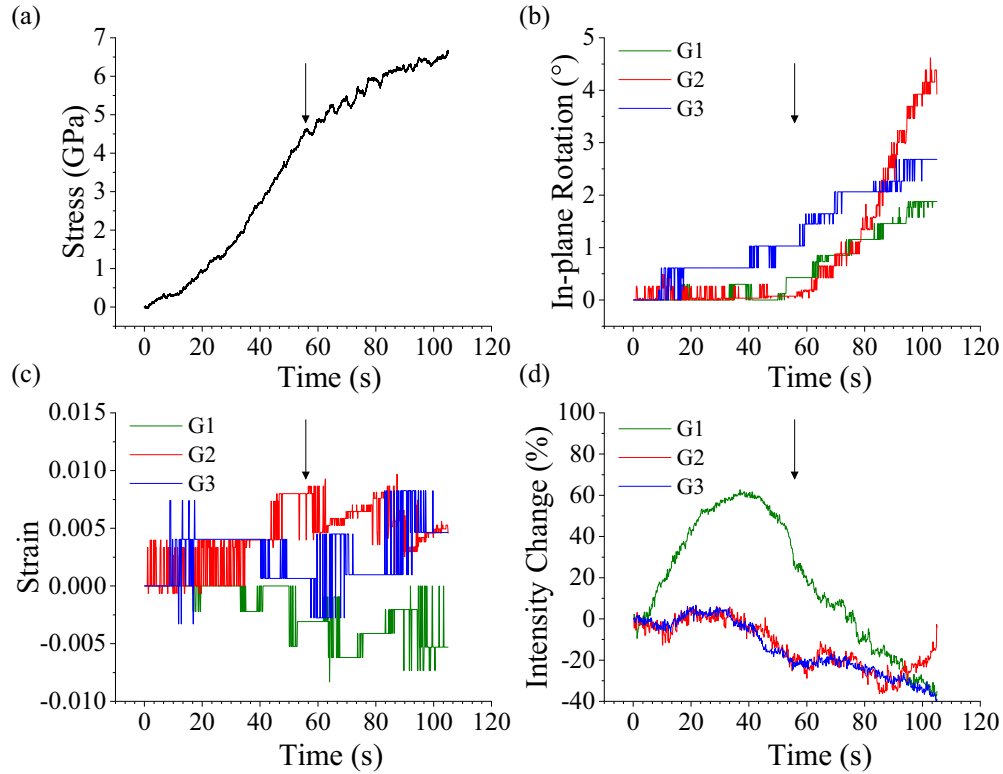
FIG. 5. Observation of grain deformation and rotation. (a) Stress-time curve of nanopillar C during compressive deformation. (b) In-plane rotation, (c) lattice strain, and (d) diffraction spot intensity change of the three nanograins with increasing time. The arrows in all four figures point the time of the yielding point in the stress-time curve.

band structure development during deformation, respectively. Shear band formation led to strain localization, which resulted

FIG. 6. The correlation map of diffraction patterns recorded during nanopillar C deformation. The pixel value at the coordinate (x, y) is the correlation coefficient of two diffraction patterns recorded at time x and y. Two width reductions of the red band are found between the turning point and the yielding point, which are indicated by two lines R1 and R2.

in further activities as we see the red band width narrow down at R1 and R2. Subsequently, the red band slightly broadened and stayed at a similar width after yielding.
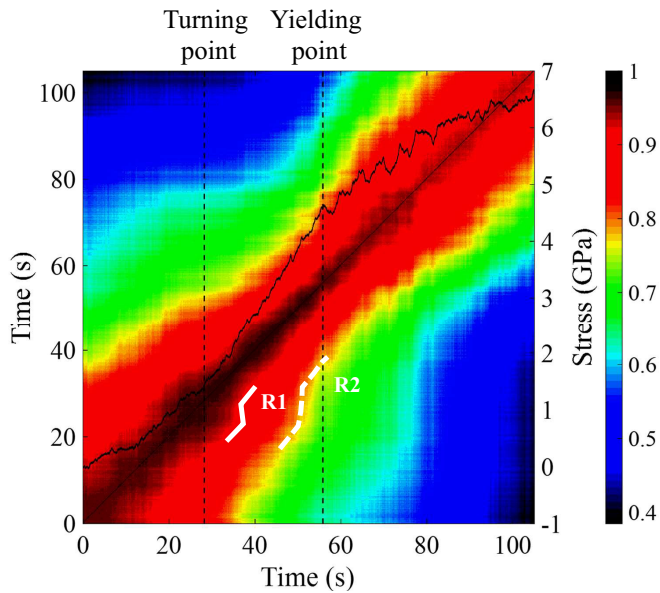
G. Stress drops caused by granular activities during deformation

A statistical analysis was performed to determine the characteristic of granular activities in 10 nanopillars before yielding. As a large granular activity or dislocation slip can lead to a sudden elastic relaxation of the indenter, which yields a stress drop or a strain burst dependent on the indenter control mode [30]. Our indentation experiments were conducted under the displacement control mode so that a stress drop is detected during a granular activity, or dislocation slip, event.

Figure 7(a) shows an example of the load-time curve before yielding, where a small region is enlarged in the inset. The square in the inset marks the enlarged area shown in Fig. 7(b). The noise in the load-time curve was filtered out by using a reference background noise data (see Fig. S5 in Ref. [27]). The filtered curve was then used to calculate the first-order derivative. We marked the point of where the slop changes from positive to negative as the start of a load drop, and vice versa for the end of a load drop. Load drop size was taken as the magnitude difference between the starting and the ending points. Load drop sizes of each nanopillar sample are converted into stress drop sizes based on the nanopillar geometry. The histogram of all stress drop sizes is shown in Fig. 7(c), which follows the log-normal distribution with the mean $= 0.029$ GPa and the standard deviation $= 0.018$ GPa.
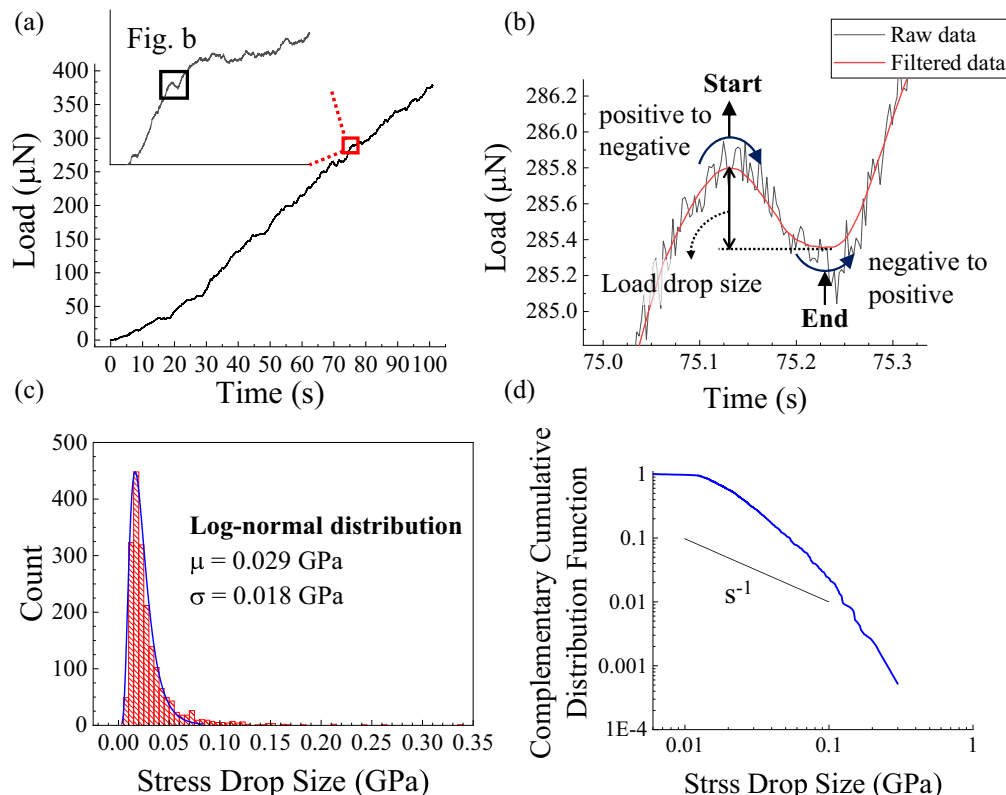
FIG. 7. Stress drops observed during nanopillar deformation. (a) An example of the load-time curve before yielding. The square in the inset figure marks the enlarged region (b). (b) An example of measuring a load drop from the filtered load-time data. (c) Histogram and (d) CCDF curve of the measured stress drop sizes from 10 nanopillars. The s^{-1} line is drawn for comparison.

To predict the deformation behavior, we also calculated the complementary cumulative distribution function (CCDF) of all the stress drop sizes occurred in 10 nanopillars based on mean field theory [31,32]. Figure 7(d) shows the CCDF curve of the stress-integrated distribution of the stress drop sizes.

IV. DISCUSSION

A. Grain size effect on dislocation avalanches

The statistics of the measured stress drops in all ten ZrN nanopillars [Fig. 7(c)] shows that the drop magnitude is relatively small (29 ± 18 MPa), while the mean yielding stress of the nanopillars is 7.2 ± 1.7 GPa.

The CCDF of the measured stress drops deviates significantly from the reported power-law behavior associated with dislocation avalanches [29,31,32]. According to mean field theory (MFT) model of solid deformation [31], a slip occurs at a weak spot as the local failure stress is exceeded and the spot will be weakened. The stress at the slip location is then redistributed and may increase the stress at other weak spots causing more slip events. The cascade of local slips leads to a slip avalanche. The avalanche stops as the stress at every spot is reduced below the failure stress. The avalanche process will give rise to a power-law distribution of slip sizes, and obtain a universal exponent of -1 as the distribution is described by CCDF. The significant deviation in the exponent can be attributed to the effect of the nanograin size. Grain boundaries are strong obstacles to dislocation movement and

thereby restrict avalanche size. Acoustic experiment on polycrystalline ice samples shows that the cutoff of power-law distribution decreases with decreasing grain size [33]. This provides a direct evidence of the effect of grain boundary on a dislocation avalanche. Simulation on the simplified polycrystalline models of different number of grains indicates that the probability of a system-spanning avalanche decreases with increasing number of grain boundaries since the barrier effect of each grain boundary is independent and accumulative [34]. However, the avalanche model may be deviated at nano scale because nanograins contain fewer dislocations. In nanograins, the previous study [35] demonstrates that the deformation is carried out by uncorrelated dislocation nucleation and propagation due to the vanished collective behavior of dislocations. This may explain the absence of avalanche. As a result, we suggest that a large volume fraction of grain boundaries strongly confine nanograin operations such that the sizes of dislocation slips during deformation are limited.

The confinement of GBs also results in intermittent granular activities. Due to the restriction, a threshold stress is required for carrying out activities. As the accumulated internal stress reaches the threshold, nanograins start to operate and simultaneously release part of the stress. The nanograins become static as the internal stress is once again below the threshold. The repeated process of stress accumulation and release intermittently enables nanograin to operate. Thus the rotational movement of a single grain intermittently progressed [Fig. 5(b)] and the overall granular activities were fluctuating during deformation [Fig. 3(b)].

B. Shear band formation

Our study shows that the failure of nanocrystalline ZrN nanopillars is dominated by shear banding. Previously, shear band formation was observed in selected polycrystalline materials during the creep rupture [36] and high-strain-rate deformation [37]. Brittle fracture is avoided in the first case by avoiding high stress, while during high-strain-rate deformation under a critical grain size, the comminution process is suppressed by particle deformation and repacking. For nanocrystalline materials, dislocation avalanches are inhibited, as our measurements show. Additionally, the internal flaw size of ceramics is usually proportional to the grain size, where the stress intensity factor at the crack tip is significantly reduced by nanograin size [38]. Therefore hindered dislocation avalanches and suppressed brittle fracture are the essential conditions of shear banding in NCCs.

The appearance of shear band features in our *in situ* videos indicates that their formation in NCCs relies on the cooperation of granular activities. In the case of shear bands (S1 and S2) in in Fig. 2(b), they are initially composed of multiple discrete bright contrast regions, indicating that several nanograins along the shear band are simultaneously operating. The cooperative process of shear band formation previously was observed in NCMs [7]. The CD images of different periods of time [Figs. 3(d) and 3(e)] show that a few nanograins operate more frequently than others along the shear band before the shear band forms, suggesting that initially the nanograins operate cooperatively to modify local microstructures. Because of the granular activities, intergranular cracks form, which has been suggested in Refs. [20,39,40]. When these cracks grow, they are directly evidenced in our experiment (Fig. S6 [27]). As local sites and intergranular cracks are modified and aligned by further granular and dislocation activities, an embryonic shear band will be formed. The idea of embryonic shear bands was previously proposed in metallic glasses, where a shear band is formed via collection and self-organization of shear transformation zones (STZ) initiated at weak sites [3]. In such scenario, the local shear stress of STZs plays an important role in shear band formation [41]. In NCC materials, we suggest that the high stress concentration at crack tips provide the local stress that drives the embryonic shear band formation. In our nanopillar compression experiments, the embryonic shear band features appeared much earlier than the yielding point, implying that the shear bands were not fully formed to carry out shear banding, and took time to complete their structure development. The development is clearly carried out by the cooperative, but physically separated, granular activities. We speculate that the stress fields of intergranular cracks must be aligned to produce such cooperation and the alignment of stress fields is critical by providing stronger interactions to induce shear band formation.

Because of the effect of maximum shear stress, intergranular crack initiation and propagation preferentially occur along a certain direction. The stress fields of intergranular cracks then become the embryos of the shear band, which also act to terminate the dislocation network propagation (Fig. 4) before shear banding. The integrated difference image up to the yielding point [Fig. 3(f)] shows most of granular activities are distributed in the region between the two shear bands and the contact surface of the nanopillar. Only a few granular activities are seen on the other side of the shear bands. Thus, the stress redistribution due to intergranular cracks leads to an inhomogeneous stress state, where the stress is higher at where the granular activities are observed. The same phenomenon has been observed in a rock model under a uniaxial compression [42]. The heterogeneity in a sample is reportedly to be associated with the localization of microfractures near the fault zone and inhomogeneous internal stress before ultimate failure. In addition, previous study [37] suggested that shear band formation in ceramics is highly related to microstructural inhomogeneities. The effects of inhomogeneities likely leads to the preferential intergranular crack initiation, while the maximum shear stress determines the propagation and the final shear banding in NCCs.

The characteristic distribution of granular activities associated with shear band formation can be defined by the cooperative activities as detected by the difference image method [Fig. 2(b)]. The involved nanograins are located near the band of thickness about 10–20 nm, which is consistent with the measured average grain size of ZrN by x-ray diffraction.

The impact of shear band formation and its development on the microstructure is also seen by electron imaging. As an embryonic shear band is formed, the localized shear stress within the band will promote further local granular activities, which leads to the connected granular activities, as seen in the difference image (Fig. 2). The first width reduction R1 of the red band in the correlation map (Fig. 6) is another evidence of accelerated granular activities. Thus, the microstructure modification is promoted by the embryonic shear band. During the shear band development, nanograins nearby the embryonic shear band are also activated, which introduces even larger microstructure modifications, resulting in a larger band width reduction R2 with shear banding (Fig. 6).

As the shear band development is completed, plastic shear is carried out and localized granular activities are greatly enhanced by shear banding. Intense plastic shear is induced within the shear band. The shear stress inside provides a large driving force for granular rotation, which are seen by our experiment [Fig. 5(b)]. Shear banding also enhances and accelerates grain deformation, including grain tilt. The accelerated granular activities lead to larger fluctuations in the stress-time curve, which is seen after yielding. The enhanced granular activities also impact the regions near the shear band, as shown in videos 2 and 3 in Ref. [27].

C. Proposed NCC nanopillar deformation model

The deformation model of NCC nanopillars according to our findings is illustrated in Figs. 8(a)–8(d). Granular activities, such as grain rotation, deformation, GB sliding, randomly occur initially to carry out plastic flow. The activities start from the volume near the nanopillar contact surface with the indenter probe because of the stress concentration of the tapered pillar [29]. As the applied stress increases, the activities flow intermittently, and random activities are seen to take place throughout the process [Fig. 8(b)]. With granular activities, the microstructure is locally modified. Because of this, intergranular cracks are initiated at weak spots, such as
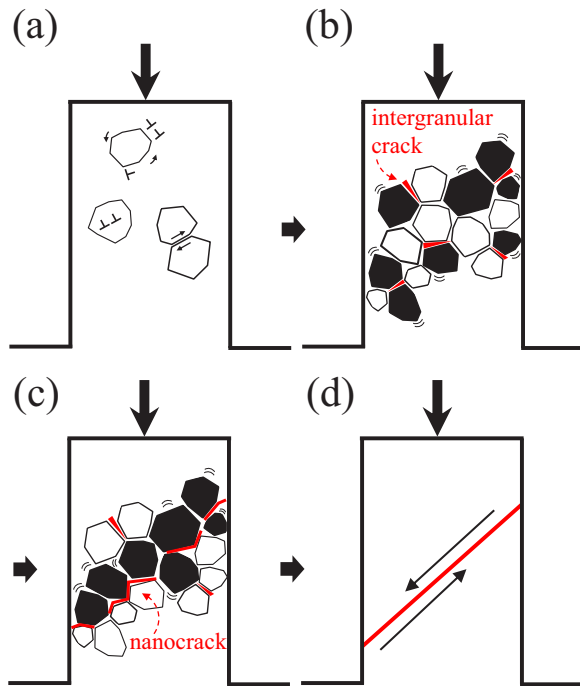
FIG. 8. The proposed shear banding model in a nanocrystalline ceramic nanopillar. [(a)–(d)] Schematic diagram of shear band formation during compression. (a) Granular activities are initiated in a nanopillar. (b) Modification of local microstructure and initiation of intergranular cracks. Black solid grains represent the grains of high activities. (c) Embryonic shear band is formed when local sites and the stress fields of intergranular cracks are aligned. Some intergranular cracks are developed into nanocracks. (d) Plastic shear is carried out as the shear band structure is completely developed.

the triple junctions and other local sites [39,40]. The intergranular cracks are most likely to form at where the dislocation and granular activities are highest. The concentration of such activities is observed near the future shear band site. An embryonic shear band is formed by the strong interactions of the aligned stress fields from intergranular cracks. These two stages [Figs. 8(b) and 8(c)] mainly occur between the turning point and the yielding point in the stress-time curve. Afterward, the structure of the embryonic shear band continues to develop by the cooperative granular activities. As the shear band development is finished, shear banding begins to dominate the deformation, which occurs after the yielding point [Fig. 8(d)].

Similar stages of shear band formation are often found in work-softening materials, such as metallic glasses and granular materials. The conventional metals are work-hardening materials. In metals, a shear band will develop into a crack or cracks (for example, see Refs. [43,44]). In the work-softening metallic glasses, the work by Qu *et al.* [45] using *ex situ* SEM on deformed samples revealed three regions of morphologies

could be associated with three stages of shear band formation, including stage I with free volume augmentation and nanoscale void formation, stage II with void growth and microcrack formation, and stage III characterized by microcrack development and final fracture. The deformation of the NCC nanopillars observed here similarly is characterized by stages of shear band formation, but with important differences that are specific to granular materials, as the initial stage is characterized by intermittent dislocation and granular activities, which lead to the development of intergranular cracks at weak spots, and the embryonic shear band develops by the cooperative granular activities. Thus intergranular cracks in NCC play the role of voids in metallic glasses.

The intergranular cracks initially are too small to be observed in TEM. The intergranular cracks develop into nanocracks with increasing load that further contribute to shear band formation. The smallest growing nanocracks that can be seen are about 7 nm in length according to Fig. S6.

V. CONCLUSIONS

In situ electron imaging and diffraction observations of granular activities and underlying dislocation mechanism associated with shear banding in the ZrN nanopillars are reported here. Results show the intermittent granular activities from the repeated stress accumulation and relieve during deformation. The stress drops due to the granular activities are measured, and results suggest that the sizes of associated dislocation activities are strongly limited by the small grain size. From the observed granular activities, we propose that intergranular cracks are initially generated from the local microstructure modifications, and their stress fields are aligned by further granular activities. An embryonic shear band is formed based on the aligned stress fields of intergranular cracks. When the shear band structure is fully developed, shear banding leads to plastic yielding. Enhanced granular activities are observed during shear banding. Our study thus reveals (1) the nature of intermittent granular activities in NCCs, (2) the strong correlation between granular activities and shear band formation, and (3) a new approach of monitoring granular activities and shear banding process in nanocrystalline materials.

[1] J. Humphreys, G. S. Rohrer, and A. Rollett, *Recrystallization and Related Annealing Phenomena*, 3rd ed. (Elsevier, Oxford, 2017), pp. 13–79.

[2] M. Chen, Annu. Rev. Mater. Res. **38**, 445 (2008).

[3] A. L. Greer, Y. Q. Cheng, and E. Ma, Mater. Sci. Eng. R Reports **74**, 71 (2013).

[4] R. O. Davis and A. P. S. Selvadurai, *Plasticity and Geomechanics* (Cambridge University Press, Cambridge, 2002).

[5] T. B. Nguyen, S. McNamara, J. Crassous, and A. Amon, EPJ Web Conf. **140**, 10001 (2017).

[6] E. Ma, Scr. Mater. **49**, 663 (2003).

[7] A. Hasnaoui, H. Van Swygenhoven, and P. M. Derlet, Science **300**, 1550 (2003).

[8] T. J. Rupert, J. Appl. Phys. **114**, 033527 (2013).

[9] J. R. Trelewicz and C. A. Schuh, Acta Mater. **55**, 5948 (2007).

[10] M. A. Meyers, A. Mishra, and D. J. Benson, Prog. Mater. Sci. **51**, 427 (2006).

[11] T. G. Nieh, J. Wadsworth, and O. D. Sherby, *Superplasticity in Metals and Ceramics* (Cambridge University Press, Cambridge, 1997), pp. 91–124.

[12] J. Karch, R. Birringer, and H. Gleiter, Nature **330**, 556 (1987).

[13] M. J. Mayo, in *Mechanical Properties and Deformation Behavior of Materials Having Ultra-Fine Microstructures*, edited by M. Nastasi, D. M. Parkin, and H. Gleiter (Springer, Netherlands, Dordrecht, 1993), pp. 361–380.

[14] R. A. Andrievski and G. V. Kalinnikov, Surf. Coat. Technol. **142–144**, 573 (2001).

[15] D. V. Shtansky, S. A. Kulinich, E. A. Levashov, A. N. Sheveiko, F. V. Kiriuhancev, and J. J. Moore, Thin Solid Films **420-421**, 330 (2002).

[16] F. Cao, H. Park, G. Bae, J. Heo, and C. Lee, J. Am. Ceram. Soc. **96**, 40 (2013).

[17] J. Schiotz and K. W. Jacobsen, Science **301**, 1357 (2003).

[18] D. Guo, S. Song, R. Luo, W. A. Goddard, M. Chen, K. M. Reddy, and Q. An, Phys. Rev. Lett. **121**, 145504 (2018).

[19] Z. B. Qi, P. Sun, F. P. Zhu, Z. C. Wang, D. L. Peng, and C. H. Wu, Surf. Coat. Technol. **205**, 3692 (2011).

[20] H. Ryou, J. W. Drazin, K. J. Wahl, S. B. Qadri, E. P. Gorzkowski, B. N. Feigelson, and J. A. Wollmershauser, ACS Nano **12**, 3083 (2018).

[21] I. Szlufarska, A. Nakano, and P. Vashishta, Science **309**, 911 (2005).

[22] T. H. Fang, W. L. Li, N. R. Tao, and K. Lu, Science **331**, 1587 (2011).

[23] L. Wang, J. Teng, P. Liu, A. Hirata, E. Ma, Z. Zhang, M. Chen, and X. Han, Nat. Commun. **5**, 4402 (2014).

[24] M. Chen, E. Ma, K. J. Hemker, H. Sheng, Y. Wang, and X. Cheng, Science **300**, 1275 (2003).

[25] D. C. Pagan, M. Obstalecki, J. Park, and M. P. Miller, Acta Mater. **147**, 133 (2018).

[26] H.-W. Hsiao, J.-H. Huang, and G.-P. Yu, Surf. Coat. Technol. **304**, 330 (2016).

[27] See Supplemental Material at http://link.aps.org/supplemental/10.1103/PhysRevMaterials.3.083601 for Supplemental Videos 1–4, Supplemental Figs. S1–S8 and Supplemental Notes 1–5.

[28] K.-H. Kim, H. Xing, J.-M. Zuo, P. Zhang, and H. Wang, Micron **71**, 39 (2015).

[29] Y. Hu, L. Shu, Q. Yang, W. Guo, P. K. Liaw, K. A. Dahmen, and J.-M. Zuo, Commun. Phys. **1**, 61 (2018).

[30] A. M. Minor, S. A. Syed Asif, Z. Shan, E. A. Stach, E. Cyrankowski, T. J. Wyrobek, and O. L. Warren, Nat. Mater. **5**, 697 (2006).

[31] K. A. Dahmen, Y. Ben-Zion, and J. T. Uhl, Phys. Rev. Lett. **102**, 175501 (2009).

[32] N. Friedman, A. T. Jennings, G. Tsekenis, J.-Y. Kim, M. Tao, J. T. Uhl, J. R. Greer, and K. A. Dahmen, Phys. Rev. Lett. **109**, 095507 (2012).

[33] T. Richeton, J. Weiss, and F. Louchet, Nat. Mater. **4**, 465 (2005).

[34] T. Niiyama and T. Shimokawa, Phys. Rev. B **94**, 140102(R) (2016).

[35] F. Louchet, J. Weiss, and T. Richeton, Phys. Rev. Lett. **97**, 075504 (2006).

[36] A. G. Evans and B. J. Dalgleish, J. Am. Ceram. Soc. **68**, 44 (1985).

[37] M. A. Meyers, V. F. Nesterenko, J. C. LaSalvia, and Q. Xue, Mater. Sci. Eng. A **317**, 204 (2001).

[38] R. W. Steinbrech, J. Eur. Ceram. Soc. **10**, 131 (1992).

[39] I. Ovid'ko and A. G. Sheinerman, Acta Mater. **52**, 1201 (2004).

[40] I. A. Ovid'ko and A. G. Sheinerman, Phys. Rev. B **77**, 054109 (2008).

[41] G. N. Yang, Y. Shao, and K. F. Yao, Sci. Rep. **6**, 21852 (2016).

[42] C. A. Tang, H. Liu, P. K. K. Lee, Y. Tsui, and L. G. Tham, Int. J. Rock Mech. Min. Sci. **37**, 555 (2000).

[43] J. F. Kalthoff, Opt. Eng. **27**, 271035 (1988).

[44] M. Zhou, A. J. Rosakis, and G. Ravichandran, Int. J. Plast. **14**, 435 (1998).

[45] R. T. Qu, F. Wu, Z.-F. Zhang, and J. Eckert, J. Mater. Res. **24**, 3130 (2009).